ACSNANO

www.acsnano.org

ARTICLE

Direct Optoelectronic Imaging of 2D Semiconductor–3D Metal Buried Interfaces

Kiyoung Jo, Pawan Kumar, Joseph Orr, Surendra B. Anantharaman, Jinshui Miao, Michael J. Motala, Arkamita Bandyopadhyay, Kim Kisslinger, Christopher Muratore, Vivek B. Shenoy, Eric A. Stach, Nicholas R. Glavin, and Deep Jariwala*

Cite This: *ACS Nano* 2021, 15, 5618–5630

Read Online

ACCESS | Metrics & More | Article Recommendations | Supporting Information

ABSTRACT: The semiconductor–metal junction is one of the most critical factors for high-performance electronic devices. In two-dimensional (2D) semiconductor devices, minimizing the voltage drop at this junction is particularly challenging and important. Despite numerous studies concerning contact resistance in 2D semiconductors, the exact nature of the buried interface under a three-dimensional (3D) metal remains unclear. Herein, we report the direct measurement of electrical and optical responses of 2D semiconductor–metal buried interfaces using a recently developed metal-assisted transfer technique to expose the buried interface, which is then directly investigated using scanning probe techniques. We characterize the spatially varying electronic and optical properties of this buried interface with <20 nm resolution. To be specific, potential, conductance, and photoluminescence at the buried metal/MoS_2 interface are correlated as a function of a variety of metal deposition conditions as well as the type of metal contacts. We observe that direct evaporation of Au on MoS_2 induces a large strain of ~5% in the MoS_2 which, coupled with charge transfer, leads to degenerate doping of the MoS_2 underneath the contact. These factors lead to improvement of contact resistance to record values of 138 kΩ μm, as measured using local conductance probes. This approach was adopted to characterize MoS_2–In/Au alloy interfaces, demonstrating contact resistance as low as 63 kΩ μm. Our results highlight that the MoS_2/metal interface is sensitive to device fabrication methods and provide a universal strategy to characterize buried contact interfaces involving 2D semiconductors.

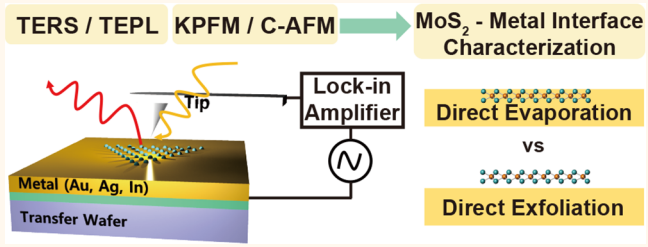

KEYWORDS: *MoS_2, two-dimensional semiconductor–metal interface, buried interface, Kelvin probe force microscopy, tip-enhanced Raman spectroscopy*

The semiconductor–metal junction is one of the most consequential for electronic and optoelectronic device performance. This junction has been a crucial bottleneck for improvement of nanoelectronic device performance and minimizing power consumption. For <20 nm channel length ballistic field-effect transistors, the voltage drop due to metal–semiconductor contact resistance is the primary source of energy dissipation and also contributes to parasitic circuit elements, thereby limiting high-frequency operation. Metal contacts for semiconductors are often imperfect due to surface effects such as Fermi level pinning, incomplete passivation of surface dangling bonds, and chemical reactivity of the metal with the semiconductor, all of which have long plagued many 3D bulk semiconductors such as Si, Ge, and the III–V family.[1−3] Traditionally, a major obstacle to understanding contact resistance has been the buried nature of the metal–semiconductor interface. This interface is confined by both the semiconductor and metal, and it is therefore impossible to directly measure electronic and optical signals and map the two-dimensional interface.

The advent of atomically thin two-dimensional (2D) semiconductors has renewed enthusiasm and interest in post-silicon channel candidates given their superior electrostatic control. In this context, the 3D metal contacts to 2D semiconducting channels are of paramount importance. However, the utility of perfect contacts stems far beyond just transistors, but also to photovoltaics, LEDs, and other optoelectronic devices.[4,5] Unlike 3D semiconductor surfaces, however, most 2D semiconductors (and the chalcogenides in

Received: January 25, 2021
Accepted: March 2, 2021
Published: March 8, 2021

https://dx.doi.org/10.1021/acsnano.1c00708
ACS Nano 2021, 15, 5618–5630

particular) have self-passivated, oxide-free surfaces. While this avoids the issue of unpassivated dangling bonds and surface oxides on the semiconductor side, it creates additional challenges in providing an electronically intimate, uniform, and low-resistance contact with 3D metals, even when the contact metal is an inert noble metal such as Au. A large body of work on bulk 3D metal/2D semiconductor contacts is available.[6−8] A number of metals with varying work functions and compositions have been investigated as electrical contacts to 2D semiconductors, namely, transition metal dichalcogenides (TMDCs) (MX_2; M = Mo, W; X = S, Se, Te), in the context of field-effect devices such as transistors.[7,8] In addition, the impact of deposition parameters and methods has also been thoroughly investigated.[8] It was found that oxide-forming metals tend to chemically react with 2D semiconductors forming unstable contacts with contact resistance increases or become nonohmic with time.[6,8,9] On the other hand, use of high-energy or lower pressure deposition methods such as e-beam evaporation or ion beam sputtering results in bombardment-induced damage, creating interface states that result in Fermi level pinning.[9,10] In such cases, the use of mechanical stamping[10] or low-melting-point metals such as indium[11] and its alloys has resulted in low-resistance contacts with pristine interfaces. Surface chemistry and phase engineering have also been employed in TMDCs on Mo and W, which induces 2H (semiconducting) to 1T′ or 1T phase transition that reduces the contact resistance with bulk 3D metals.[12−14] This phase transition can be induced *via* lithium intercalation,[13] local heating,[15] or even using local electron beam irradiation.[16] Thus, significant research has been performed on making high-quality contacts between 3D metals and 2D semiconductors.

In terms of characterizing this 3D metal/ 2D semiconductor buried interface, prior research has largely focused on localized structure measurement *via* cross-sectional transmission electron microscopy (TEM)[10] or Raman spectroscopy of evaporated metal nanoislands[17,18] on the 2D semiconductor. Several studies on current−voltage responses on field-effect devices[10] have also been conducted, but such measurements are indirect and ensemble in nature.

Scanning probe micro-spectroscopy with a tip-based local probe is a powerful technique for comprehensive nanoscale characterization, as it can provide optical, electrical, and structural information on the surface with high spatial resolution and is only limited by the tip sharpness or diameter.[19] The tip-based local probe not only allows mapping of local topography and electrical properties, but by taking advantage of the ultrasharp apex of the metal tips, also allows concurrent probing of optical properties *via* the plasmonic gap mode that is formed between the tip and a plasmonic substrate. The gap mode further helps enhance optical signals by virtue of the high local electric fields and the Purcell effect for photoluminescence and Raman scattering phenomena. These combined features enable a multifunctional, non-destructive, and versatile technique to probe optoelectronic interfaces. Several studies on 2D TMDCs using such scanning local-probe micro-spectroscopies have been already performed, including correlation of optical and electronic properties at crystal defects.[20,21] However, to the best of our knowledge this multifunctional technique has not been used to characterize and understand the buried metal−semiconductor interface.

In this study, we investigate the MoS_2−metal buried interface directly *via* the tip-based scanning probe technique. By correlating electronic techniques such as Kelvin probe force microscopy (KPFM) and conductive AFM (C-AFM) with optical information such as tip-enhanced Raman (TERS) and photoluminescence spectroscopy (TEPL), we have comprehensively evaluated electronic, optical, and mechanical properties of the buried interface, all concurrently measured with high spatial resolution (tens of nanometers). Our studies have also provided insight into MoS_2−metal interfaces formed *via* various metal deposition techniques as well as different metals. Our results highlight that metal contacts formed *via* evaporation are distinct as compared to van der Waals contacts and that In/Au alloy-based evaporated contacts offer the lowest resistance concurrently with high spatial homogeneity.

RESULTS AND DISCUSSION

To investigate optical and electrical properties of a 2D semiconductor−metal interface, MoS_2 was used as a representative 2D semiconductor. To correlate optical and electrical properties, the scanning probe technique was used (Figure 1a). Specifically, TERS and TEPL spectra were

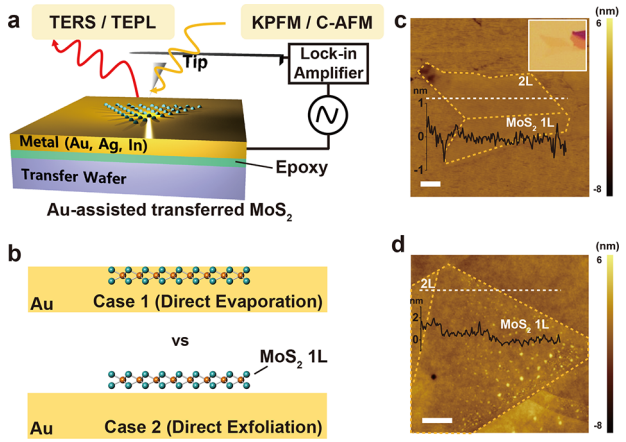

Figure 1. (a) Schematic representation of scanning probe techniques used in this study including KPFM, C-AFM, tip-enhanced Raman, and PL spectroscopy (b) Cross-sectional view of Au-assisted transfer of monolayer (1L) MoS_2 (top, referred to as case 1) for directly evaporated metal contacts and directly exfoliated MoS_2 on Au (bottom, case 2) that are investigated in this study. (c, d) Topography map of (c) case 1 and (d) case 2. Inset in (c) is an optical image of the MoS_2 flake transferred after direct Au evaporation. Graphs inside (c) and (d) represent the lateral height profile along white dotted lines. Scale bars indicate 1 μm.

obtained. In addition, KPFM and C-AFM were performed as electrical characterization on the same flake to avoid possible sample-to-sample variation. To characterize and compare the properties of two different types of interfaces, samples were prepared as follows. (i) Case 1 (direct evaporation) interface: direct evaporation of Au on MoS_2 followed by epoxy-assisted template stripping to expose the buried interface. (ii) Case 2 (direct exfoliation) interface: direct mechanical exfoliation of MoS_2 on freshly template stripped Au films as shown in Figure 1b. The electron beam evaporation technique was used to deposit Au (see Methods and Figure S9).[22] Thermal evaporation and sputtering were also investigated (see Supporting Information S8 for details). Due to the high kinetic energy of incoming Au atoms during evaporation, Au atoms are likely to strongly couple with S atoms on the MoS_2 surface, leading to an intimate electronic contact with

https://dx.doi.org/10.1021/acsnano.1c00708
ACS Nano 2021, 15, 5618−5630

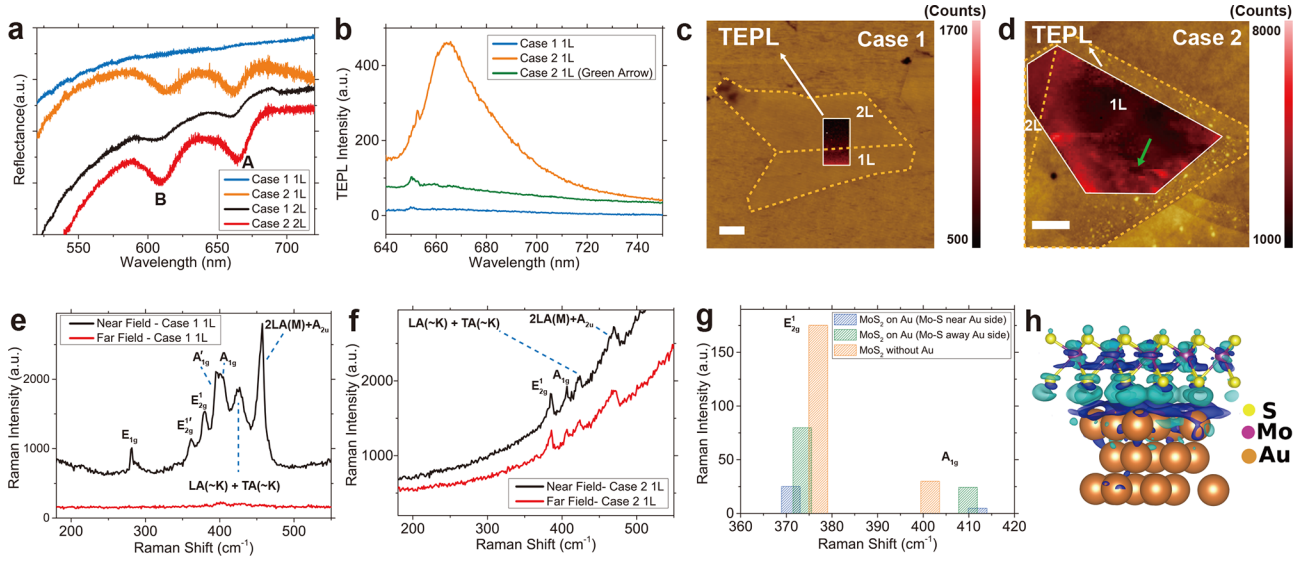

Figure 2. (a) Reflectance spectra of cases 1 and 2 with either monolayer (1L) or bilayer (2L) MoS_2. (b) Tip-enhanced photoluminescence (TEPL) spectrum of cases 1 and 2 with monolayer MoS_2. The orange and green spectra are from two separate points on the directly exfoliated MoS_2. The green spectrum was collected at the location indicated by the green arrow shown in (d) at a quenched region. (c, d) TEPL map of (c) case 1 and (d) case 2. Scale bars indicate 1 μm. (e, f) Near-field (black) and far-field (red) Raman spectrum of (e) case 1 and (f) case 2 with monolayer MoS_2. (g) First-principles calculation of peak intensities of the two characteristic Raman modes of MoS_2 with and without a Au layer. The distinct blue and green bars result from the asymmetric Mo−S bond length change due to single-sided contact of MoS_2 with the Au layer in the calculated model. (h) Charge density difference map between the MoS_2 and Au(111) surface. Dark blue and light blue stand for loss and gain of charge density, respectively.

negligible tunneling or Schottky barriers. On the other hand, it is widely accepted that the 2D TMDC semiconductor−metal van der Waals (vdW) interface consists of tunneling and Schottky barriers because MoS_2 only forms a physical junction with Au without chemical bond formation.[23] Therefore, these two representative samples serve as a good comparison to understand the TMDC−metal interface. Topography analysis of the case 1 (direct evaporation) interface clearly reveals a flat height profile of the MoS_2 flake, indistinguishable from surrounding Au with minimal surface roughness (0.188 nm rms on flake *vs* 0.330 off flake). For the case 2 (direct exfoliation) interface, the MoS_2 sits atop the Au and, hence, shows clear atomic steps and thickness variance with increased roughness (0.734 nm on flake *vs* 0.368 off flake) in AFM topography. These AFM topography results suggest that direct metal evaporation offers a more spatially uniform contact.

The presence of strongly bound excitonic resonances in 2D TMDCs also provides an additional probe of the surrounding dielectric medium. In a metal−2D MoS_2 contact this can therefore be probed *via* far-field reflection spectroscopy. Figure 2a shows representative reflectance measurement of each contact. The monolayer and bilayer MoS_2 case 2 (direct exfoliation) interface clearly shows two reflectance dips corresponding to A and B excitonic absorption at ∼660 and ∼610 nm, respectively.[24,25] On the contrary, the excitonic peaks were suppressed in the case 1 (direct evaporation) interface. For the case of monolayer MoS_2 with direct Au evaporation there is no clear evidence of excitonic resonances. This is particularly interesting because it has been reported that weak excitonic absorption peaks arise even in nanocrystalline MoS_2.[26] The complete disappearance of the excitonic transitions from a single crystalline exfoliated flake suggests that the degenerate doping *via* the evaporated metal contact is strong enough to completely screen out exciton formation by virtue of Pauli blocking. This further suggests that the monolayer MoS_2 surface is metallized or degenerately doped by the bottom Au contact. This result also shows that the Au-based transfer technique is powerful for preparation of metallized TMDC layers. For the bilayer sample, however, the excitonic peaks reappear at ∼661 and ∼607 nm, respectively, for the A and B exciton. This further suggests that the metal-induced degenerate doping is a strong function of separation from the metal, and therefore the second layer in bilayer sample shows evidence of excitons. However, the peaks are broader and weaker compared to directly exfoliated samples, which is an indication of charge transfer from the metal.

The scanning probe tip can also be effectively used as an antenna to obtain reliable, tip-enhanced Raman and photoluminescence signals[27,28] from these MoS_2−Au samples. Good electrical contact of a metal with a 2D semiconductor such as MoS_2 should result in degenerate doping that would lead to photoluminescence suppression since high carrier density drives nonradiative recombination of excitons.[29]

TEPL was therefore conducted to understand excitonic emission for each MoS_2−Au interface. Overall, the photoluminescence (PL) intensity from MoS_2 for case 1 (direct evaporation) is largely suppressed compared to that of the case 2 (direct exfoliation) interface (Figure 2b,c,d). This clearly demonstrates that the buried interface formed *via* direct metal evaporation makes an electrically good contact in agreement with the reflectance results. This suppression can be explained by first-principles calculation of the band structure of MoS_2 in the vicinity of Au, which we will discuss later. Another possibility is that the TEPL is quenched by quantum tunneling and nonlocal screening where the gap distance is <1 nm.[30,31] This further shows that the MoS_2−Au distance in the case 1 (direct evaporation) interface is small enough to consider quantum plasmonic effects and further illustrates the physical and electronic intimacy of the contact. On the other hand, the

https://dx.doi.org/10.1021/acsnano.1c00708
ACS Nano 2021, 15, 5618−5630

case 2 (direct exfoliation) samples emit high PL intensity at 665 nm, which is the optical band gap of MoS_2. This implies that the physical proximity with metal does not effectively quench the excitons in MoS_2 since the interface contains a small vdW gap. Further, it is clearly evident that the PL is spatially varying. To be specific, this large spatial inhomogeneity in PL is indicative of spatial inhomogeneity in the electronic quality of the MoS_2−Au contact with certain "electrically active" regions (indicated by a green arrow in Figure 2d) of ∼500 nm in lateral size showing reduced PL, suggesting that these "electrically active" regions are in relatively good (high-conductance) contact with the Au.

Raman spectroscopy is another powerful tool to characterize 2D crystals including semiquantitative analysis of carrier density and strain.[18,32−34] Coupled with a tip-based scanning probe technique, tip-enhanced Raman spectroscopy can resolve Raman scattering with high spatial resolution. In a TERS system, an inhomogeneous plasmonic field in the vicinity of the tip takes an important role in enhancing the intensity of the Raman signal from tens of nanometer sized regions. A variety of mechanisms[35] have been proposed for such enhancement of signal intensity. These include nonclassical plasmonic response,[31,36] molecular polarization by localized field gradients,[37] multiple elastic scatterings *via* self-interaction of the sample,[38] vibration mode−plasmon coupling,[39,40] and also chemical reactions.[41] Recent work has also shown that corrugations on the metallic tip contribute to optical rectification and molecular charging during TERS measurement.[42,43] We have investigated TERS for the case 1 (direct evaporation) and case 2 (direct exfoliation) MoS_2−Au contact interfaces (Figure 2e,f).

To the best of our understanding, the tip-induced plasmonic electric field focusing combined with a resonance Raman effect induces the observed increase in Raman scattering on the monolayer MoS_2 case 1 (direct evaporation) interface. With a sufficiently small MoS_2−Au distance in the case 1 (direct evaporation) interface, the TERS signal can be enhanced even though TEPL is quenched by quantum tunneling and nonlocal effects.[30,31] The Raman scattering is an instant relaxation process, and hence it is not affected by quantum tunneling but by the electric field intensity in the gap mode.[31] Since the gap mode electric field intensity is maintained even when the distance is <1 nm, the TERS signal can be enhanced without quenching. In this regard, the TERS measurement further gives rise to multiple peaks as shown in Figure 2e, which can also be explained by vibration mode−plasmon coupling.[39,40,44] The second-order zone-edge phonon 2LA(M) mode and first-order optical phonon A_{2u} mode arising at ∼456 cm^{-1} were observed and were due to plasmonic enhancement.[18] In-plane mode E_{1g}, which is normally forbidden in the backscattering Raman process, also arises in this system as previously reported.[17,34] More importantly, strain-induced peak splitting of E^1_{2g} and A_{1g} modes appears for MoS_2 with directly evaporated Au contacts.[18,45] The presence of peak splitting is attributed to a change of symmetry from D_{3h} to C_s for the monolayer and from D_{6h} to C_{2h} for the bilayer.[18] A linear relationship of Raman peak position was reported to demonstrate a shift of 4.5 cm^{-1}/% strain for the $E^{1'}_{2g}$ mode and 1.0 cm^{-1}/% strain for the A_{1g} mode.[45] The two shifting rates were well matched with the shift of $E^{1'}_{2g}$ and E^1_{2g} modes obtained in this work, both of which suggest a ∼5.5% strain on the surface. This is considerably higher than other reports of ∼2.0% for a Ag dendrite−MoS_2 interface, 3.0% for a MoS_2−Au nanoisland, and ∼1.7% for Ag-coated CVD-grown MoS_2.[17,18,46] These differences can be attributed to many factors such as different metal layer compositions, metal morphology, and the corresponding contact area between the metal and semiconductor. This large strain can be attributed to the lattice mismatch between the Au and MoS_2. Interestingly, the monolayer MoS_2 case 1 (direct evaporation) interface did not exhibit clear Raman peaks under far-field Raman measurements that were collected by retracting the tip away by ∼30 nm from the samples. The Raman intensity suppression is likely due to intimate Au contact, which holds MoS_2 atoms tightly, hindering vibration for each atom. Besides, intimate Au contact induces high carrier concentration on MoS_2, leading to the Raman suppression as reported in previous gate-dependent far-field Raman studies.[33] The Raman spectra for the case 1 (direct evaporation) interface further suggest that there is no electronic or structural transformation in the MoS_2 upon metal evaporation, and the contact formation only induces strong degenerate doping and strain in the MoS_2 layer. On the other hand, the Raman spectrum of the monolayer MoS_2 case 2 (direct exfoliation) interface showed negligible strain, maintaining the unstrained E^1_{2g} peak position at 385 cm^{-1}.[45] It implies that MoS_2 and Au do not strongly couple, but physisorption governs the contact which does not impose enough strain that is measurable *via* Raman. This contrast clearly shows the case 1 (direct evaporation) interface is fundamentally different from the case 2 (direct exfoliation) interface in terms of strain.

Another independent factor that contributes to the electrical contact at a metal−semiconductor interface is charge transfer. Semiconductor band bending will result in the accumulation of surface charge. This charge can be qualitatively analyzed by the A_{1g} mode, which is the out-of-plane Raman mode strongly affected by electron−phonon interaction and results in softening and broadening at high electron density in MoS_2 for resonant Raman.[32,33] This is because high carrier density leads to Pauli blocking at the K point in the conduction band of MoS_2, resulting in reduced oscillator strength of the exciton.[33] In our work, the A_{1g} mode is observed to soften and widen (402 cm^{-1}) at the monolayer MoS_2 case 1 (direct evaporation) interface compared to that (406 cm^{-1}) of the case 2 (direct exfoliation) interface. We rule out the possibility of phase transition to metallic 1T MoS_2 since no discernible peaks related to the 1T phase emerge in the range of 100−350 cm^{-1} in addition to the above-discussed reasons.[47,48] Considering this, we conclude that the monolayer MoS_2 interface with directly evaporated Au is degenerately doped, while the MoS_2 interface with transferred Au is not.

To verify our Raman analysis, we performed first-principles calculations using density functional theory (DFT) of the Raman modes for MoS_2 with and without a Au layer (Figure 2g). The strength of the interaction between the MoS_2 and the metal surface was modeled by varying the distance between the surfaces and computing the interaction energy using van der Waals corrected DFT (see Methods). Bader charge analysis suggests an increase in charge transfer with decreasing interlayer distance, and as a result, a modified Fermi level emerges for MoS_2. The electronic properties of the MoS_2 also change in the presence of a metal surface. The direct band gap (∼1.66 eV) semiconductor MoS_2, due to the presence of local strain and charge transfer from the surface, turns into an indirect band gap (∼1.44 eV) semiconductor with reduction of the band gap for an interlayer separation of 2.54 Å. This

https://dx.doi.org/10.1021/acsnano.1c00708
ACS Nano 2021, 15, 5618−5630

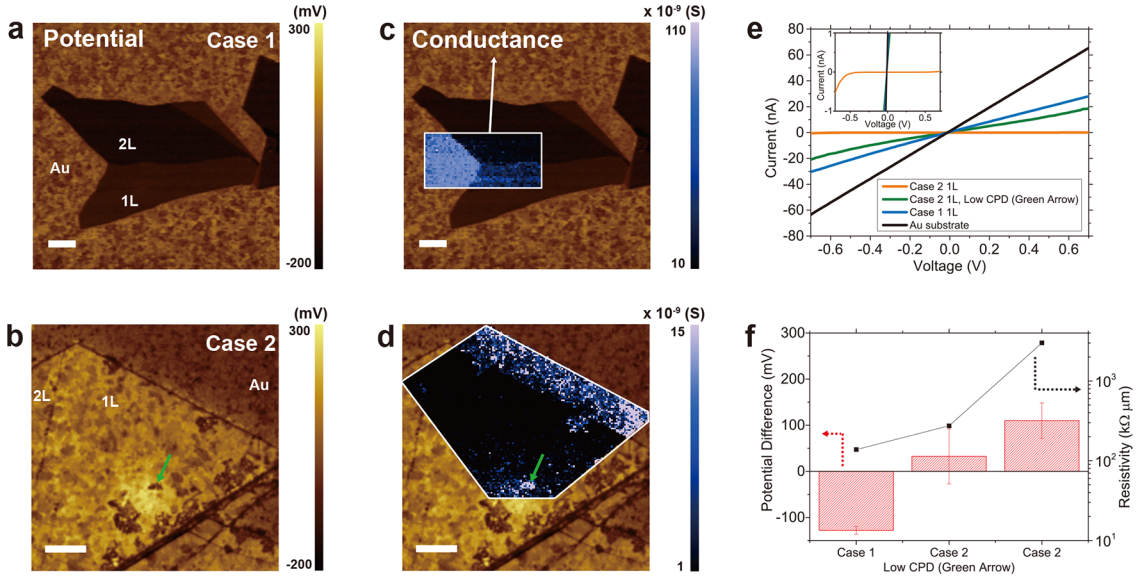

Figure 3. (a, b) Surface potential maps, (c, d) conductance mapping at −0.6 to −0.7 V of (a, c) the case 1 and (b, d) the case 2 interface. The green arrows in (b) and (d) indicate the identical position of the low-potential region. (e) *I*−*V* curves and (f) potential difference between the Au substrate and each interface plotted with corresponding resistivity. Scale bars indicate 1 μm.

computational result is in agreement with the suppressed photoluminescence spectrum of the case 1 (direct evaporation) interface (Figure 2b). In addition, the intimate contact with Au alters the Mo−S bond length depending upon which side of the MoS_2 surface is considered (the MoS_2 surface adjacent to or on the opposite side of the Au layer). As a result, the Raman intensities of E^1_{2g} and A_{1g} are highly suppressed (Figure 2g) near the Au, which coincides with our far-field Raman spectrum (Figure 2e). We note that Mo−S bonds are spatially varying along the layer thickness due to the presence of a Au layer on only one side, leading to slight shifts of E^1_{2g} and A_{1g} modes in MoS_2−Au contact (green and blue bars in Figure 2g). In addition, charge density differences also proved strong electronic coupling between MoS_2 and Au by charge transfer (Figure 2h). Significant charge transfer ($\sim 0.4e^-$) occurs from Au to the vacant *d*-orbitals of the chalcogen atoms of MoS_2. The calculation result verifies that the charge transfer and the strain play a critical role in the quality, and hence electrical and optical properties, of the MoS_2−Au contact.

Surface potentials of the monolayer MoS_2 case 1 (direct evaporation) and the case 2 (direct exfoliation) interface were investigated by KPFM. KPFM measures the potential difference between a sharp tip in the proximity of a solid surface to obtain the work function difference for the solid. The potential at the 2D semiconductor−metal interface arises from both effects of charge transfer at the interface as well as the band structure of the semiconductor. Naturally, an interface dipole can be formed due to charges in the semiconductor and the mirror image at metal. Moreover, since the MoS_2 thickness is much smaller than that of the Thomas−Fermi screen length of 3 nm along the *z*-direction, the potential due to the interface dipole is not screened out (see Supplementary Figure S3).[49] Therefore, we can directly measure the potential contributions by charge transfer at the MoS_2−metal contact. We observe stark differences in our potential maps of MoS_2−Au interfaces for the two different types of contacts being investigated. The case 1 (direct evaporation) interface exhibits lower potential than the Au substrate, while the case 2 (direct exfoliation) interface exhibits higher potential as compared to Au. The comparative potential difference ($V_{\text{interface}} - V_{\text{Au substrate}}$) is shown in Figure 3f. The potential difference of the monolayer MoS_2 case 1 (direct evaporation) interface compared to the Au substrate is recorded to be -127 ± 8.73 mV, and the corresponding work function of the monolayer MoS_2 was 5.29 eV, which is larger than the Au substrate (Figure 3a,f). As we discuss above, a considerable strain of ∼5.5% is imposed on MoS_2 underlying the directly evaporated Au. Prior theoretical estimates have suggested that strained MoS_2 with 4% biaxial (tensile) strain can eliminate any Schottky barriers since the conduction band minimum shifts below the Fermi level due to the increase of electron affinity.[23] Further, it was also reported that electron affinity of monolayer MoS_2 linearly changes as a function of strain to a value of 5.40 eV for ∼5.5% strain. This should result in a shift of conduction band minimum far below the Fermi level considering the measured work function value of 5.29 eV. Since electron affinity is higher than the work function of Au, the Schottky barrier height becomes negative according to the Schottky−Mott model. However, the Fermi level must be identical throughout the entire region; hence negative charges must accumulate on the MoS_2 side (see Supplementary Figure S3a). Assuming the type of charge induced by the MoS_2 dipole dominates the potential due to high order potential $\sim z^{-3}$, where *z* is distance, we can extrapolate that negative dipole charges are the dominant contributors to the potential measurement on the case 1 (direct evaporation) interface. Qualitatively, we can interpret the negative potential difference of −127 mV is attributed to the negative dipole at the MoS_2 side of the interface (Figure 2h and Figure S3a,b). In this respect, the surface charge of the interface was readily predicted by KPFM. Therefore, we conclude that MoS_2 is degenerately *n*-doped mainly because of biaxial strain and a partial contribution of the negative interface dipole. *n*-Type conduction at the MoS_2−Au interface is widely accepted and consistent with previous predictions by calculation.[50,51] The ohmic behavior at the case 1 (direct evaporation) interface is consistent with previous predictions of ohmic behavior in clean electrical contacts.[52]

https://dx.doi.org/10.1021/acsnano.1c00708
ACS Nano 2021, 15, 5618−5630

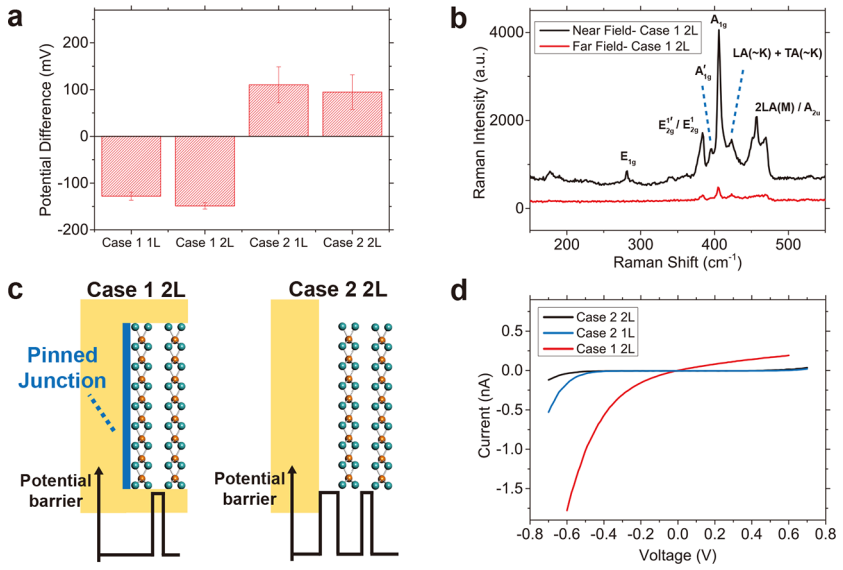

Figure 4. (a) Layer dependency of surface potential of MoS_2 with respect to the Au substrate and (b) near-field and far-field Raman spectrum of the bilayer MoS_2 case 1 interface. (c) Schematic diagram illustrating the barrier potential and (d) $I-V$ curves of the bilayer MoS_2 case 1 and the case 2 interfaces.

On the other hand, the monolayer MoS_2 case 2 (direct exfoliation) interface shows a positive potential difference of +110 ± 38.6 mV and a work function of 5.05 eV (Figure 3b,f). As per the discussion above, ∼0% strained MoS_2 should have an electron affinity of 4.59 eV according to the literature.[23] Considering the Au work function of 5.16 eV (see Methods), a Schottky barrier is formed at this interface. Following the same reasoning presented above, positive charges collect on the MoS_2 side of the interface (see Supplementary Figure S3c,d). Hence it proves that the vdW maintains *n*-type semiconducting behavior but creates a resistive Schottky barrier type contact. Similar behavior was observed in the bilayer regions shown in Figure 3c,d and are discussed in more detail later.

The stark contrast between the case 1 (direct evaporation) and case 2 (direct exfoliation) interface is attributed to coupling between Au and S atoms. The overlap between *d*-orbitals of Au and MoS_2 is critical for contact.[50] This is because d-orbitals far overwhelm the *sp*-orbitals in terms of density of states. Therefore, the distance between Au and S atoms can considerably change the conductivity or resistivity across the interface. Due to different coupling strength, not only the strain on the MoS_2 surface but also the dipole direction of the interface is changed. This interface effect emerges uniformly throughout the whole case 1 (direct evaporation) interface, which results in a spatially uniform surface potential on the monolayer and the bilayer MoS_2. Interestingly, the monolayer MoS_2 region shows uniform potential throughout the flake, despite deviation of the potential value for Au itself (+28.7 ± 33.5 mV). Note that the Au substrate also shows spatial variation of its potential value due to the polycrystalline nature of evaporated Au.[53] The spatially uniform potential of the monolayer MoS_2 in the case 1 (direct evaporation) interface indicates that the electrical response of Au is mostly screened by the free carriers of MoS_2, regardless of preoccupied surface states. On the other hand, the monolayer MoS_2 in the case 2 (direct exfoliation) interface exhibits pronounced nonuniformity in surface potential distribution. This nonuniformity is attributed to the spatially varying MoS_2−Au distance and correspondingly uneven dipole distribution. This agrees with the TEPL map (Figure 2d) showing that junction quality between Au and sample is randomized due to the spatially varying MoS_2−Au distance. Interestingly, some regions of the case 2 (direct exfoliation) interface recorded dramatically low potential, +32.6 ± 59.6 mV (green arrow in Figure 3b). We interpret this as reduction of the Schottky barrier in these regions, resulting in higher conductivity.

Accordingly, the $I-V$ response and conductance maps were collected for each interface under consideration here (Figure 3c,d,e). $I-V$ curves measured by C-AFM describe out-of-plane carrier transport. Therefore, this can serve as a measure of direct carrier injection at a 2D semiconductor−metal interface. Figure 3e represents spatially averaged $I-V$ curves (6 × 6 points). The monolayer MoS_2 case 1 (direct evaporation) interface showed a linear response of current to voltage, indicative of ohmic behavior. It is also consistent with potential map and reflectance measurements, further confirming our conclusion of degenerate doping due to direct Au evaporation. Similar to potential and TEPL maps, the case 1 (direct evaporation) interface also shows good spatial uniformity of conductance. Prior research has provided some evidence using cross-sectional TEM imaging that direct metal evaporation leads to creation of point defects, metal diffusion, broken layers of the 2D chalcogenide, and glassy layers at the evaporated MoS_2−Au interface.[10] The authors attributed these defects to the bombardment by the high-energy Au atoms on the MoS_2 surface. We do not find any evidence of such defects or Au diffusion through the MoS_2 in the potential and conductance maps acquired by scanning probe. We have also performed cross-section TEM imaging to verify our claims (see Supplementary Figure S4). On the other hand, most of the monolayer MoS_2 case 2 (direct exfoliation) interface was highly resistive and showed rectifying behavior due to the presence of tunnel and Schottky barriers. This implies an obvious relationship between conductivity and potential at the interface (Figure 3f). We extracted out-of-plane resistivity from $I-V$ curves, and contact area was obtained by using a Hertzian contact model (see Methods). Based on our calculation, the monolayer MoS_2 case 1 (direct evaporation) interface reaches

https://dx.doi.org/10.1021/acsnano.1c00708
ACS Nano 2021, 15, 5618−5630

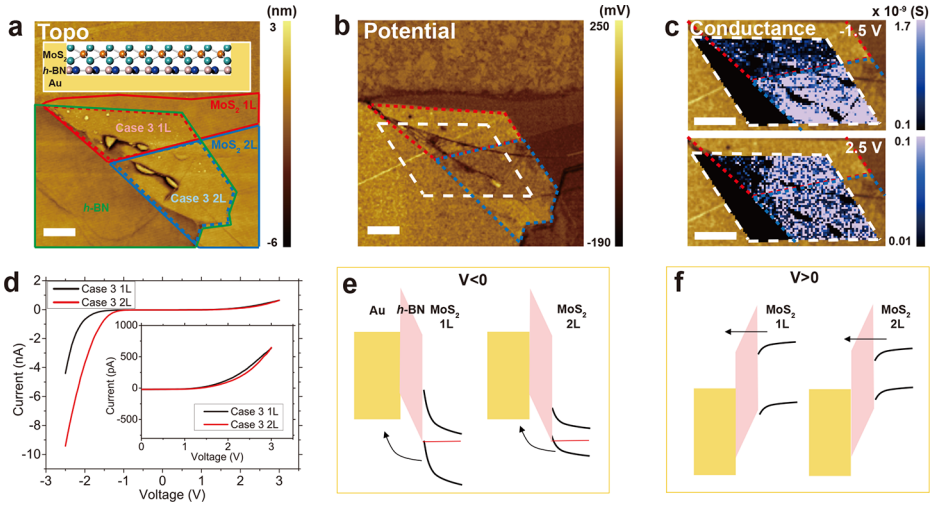

Figure 5. (a) Topography of the MoS_2/*h*-BN/Au interface (case 3). Inset in (a) is a schematic representation of the case 3 interface. Red dotted lines correspond to the monolayer MoS_2 case 3, while blue dotted lines correspond to the bilayer MoS_2 case 3 interface. (b) Surface potential (c) conductance map of the case 3 interface with (top) −1.5 V and (bottom) +2.5 V in the area covered by a white dashed line in (b). Background is the potential map. (d) *I*−*V* curves of the mono- and bilayer case 3 interface. (e, f) Band diagram of the case 3 interface at (e) $V < 0$ and (f) $V > 0$. Scale bar in all panels indicates 1 μm. Solid lines in (a) indicate monolayer MoS_2 (red), bilayer MoS_2 (blue), and *h*-BN (green).

138 kΩ μm (potential difference of −127 mV), while the case 2 (direct exfoliation) interface recorded 3,009 kΩ μm (potential difference of +110 mV). It is worth nothing that there are localized low-potential regions on the case 2 (direct exfoliation) interface (green arrow) that exhibit a linear *I*−*V* relationship and comparable conductance to that of the case 1 (direct evaporation) interface. The resistivity of these localized regions at the monolayer MoS_2 case 2 (direct exfoliation) interface was determined to be 274 kΩ μm (potential difference of +32.6 mV).

It is also worth noting that we do not find any evidence of tears, cracks, holes, or other defects in topographic images of the sample at these locations of low potential/high conductance. Therefore, we attribute these local "electrically active regions" of low potential/high conductance to high strain and/or interfacial charge that is randomly accumulated in the process of mechanical exfoliation.

To further understand the impact of these two different types of contact formation processes between MoS_2 and Au, we investigate the dependence of the number of MoS_2 layers on the Raman spectra and conductance of these contact interfaces. Bilayer MoS_2 presents an interesting case study to understand this further since a bilayer consists of two monolayers in two different surrounding environments; one layer is in direct contact with Au, while the other layer is in contact with the first layer and faces the surface. Therefore, we expect large changes in electrical properties between the two types of contact samples considered above. Figure 4a represents the potential difference of each contact interface comparing the monolayer and the bilayer MoS_2. Overall, the bilayer shows a small negative shift in potential regardless of interface type. We interpret that this shift is caused by layer-dependent band offset and changes in the band gap. Considering that the doping concentration remains the same throughout the flake, the Fermi level in bilayer MoS_2 must shift in response to the reduction in band gap. Per literature precedent, the bilayer conduction band drops by 0.1 eV and the valence band moves up by 0.2 eV as compared to the monolayer MoS_2.[54] Therefore, the electron affinity and work function of bilayer MoS_2 increase and the corresponding surface potential drops. Quantitatively, potential shifts of −20.8 and −15.6 mV were observed for the bilayer MoS_2 case 1 (direct evaporation) interface and the case 2 (direct exfoliation) interface, respectively. Moreover, the sign of the potential difference in bilayer MoS_2 samples (−148 ± 6.93 mV for case 1 *vs* +94.6 ± 37.0 mV for case 2) was the same as the monolayers for the same type of contact.

Once again TERS was used to investigate the degree of strain in bilayer MoS_2 under directly evaporated Au. Similar to monolayer MoS_2, strain-induced peak separation was analyzed, and a compressive strain of 1% was deduced based on prior reports of strain *vs* Raman peak shift relations (Figure 4b, Supplementary Figure S2c, and Table S1).[45] Compared to the 5.5% strain estimated in monolayer MoS_2 buried under directly evaporated Au, the strain in the bilayer is considerably suppressed. This can be attributed to the weak interlayer coupling in between MoS_2 layers of a bilayer sample, which helps relieve some strain.

Out-of-plane conductance measurements of bilayer MoS_2 (Figure 4d) samples on Au add further insights and evidence to the above claims. The bilayer MoS_2 case 1 (direct evaporation) interface only includes interlayer spacing (Figure 4c, left) with a pinned junction due to strong coupling between Au and S. On the other hand, the bilayer MoS_2 case 2 (direct exfoliation) interface shows rectifying behavior from two layers of potential barriers in series (Figure 4c, right). Since both junctions act as tunneling barriers for the bilayer MoS_2 case 2 (direct exfoliation) interface, current is reduced compared to the monolayer MoS_2 case 2 (direct exfoliation) interface. Strikingly, the bilayer MoS_2 case 1 (direct evaporation) interface shows a high increase in current for the same driving voltage and a linear ohmic contact like behavior. This can be understood by considering a weakly coupled semiconductor layer to a pinned, degenerately doped semiconductor with a high work function (Figure 4c, left). This type of contact may comprise relatively narrow Schottky and tunnel barriers that do

https://dx.doi.org/10.1021/acsnano.1c00708
ACS Nano 2021, 15, 5618−5630

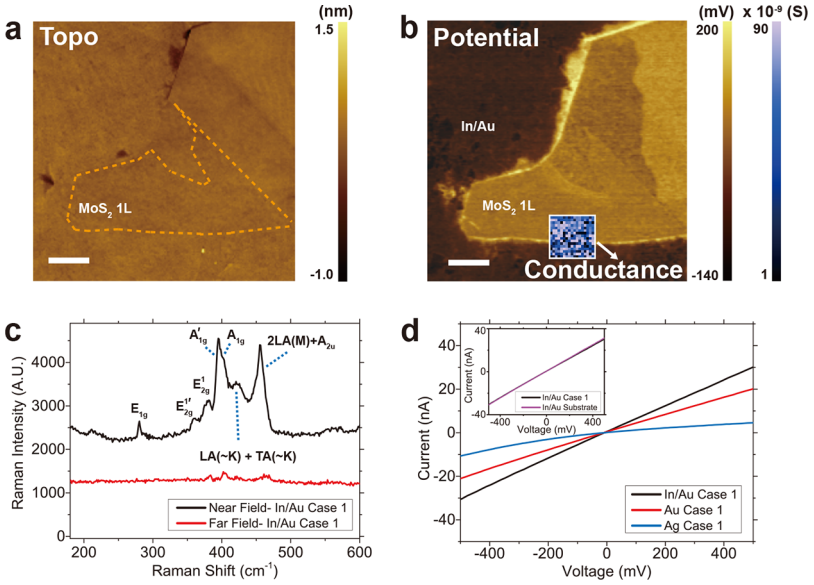

Figure 6. (a) Topography, (b) surface potential and conductance map, (c) near-field and far-field Raman spectrum, and (d) $I-V$ curves of a monolayer MoS_2−In/Au case 1 interface (the region surrounded by an orange dotted line in (a)). Inset is an $I-V$ curve comparison of the MoS_2−In/Au case 1 interface and In/Au substrate. The spatial conductance map was extracted using a voltage range of −0.4 to −0.5 V. Scale bar in (a) indicates 1 μm.

not produce much rectifying behavior, resulting in efficient charge injection and low-contact resistance.[51,55]

To further understand the nature of the buried interface between directly evaporated Au and MoS_2, we need to develop a way to tailor/modify this interface to eliminate this degenerate doping of the monolayer in immediate proximity to MoS_2 and depin the Fermi level. As discussed above, Fermi level pinning is one of the critical challenges to address in 2D semiconductor/3D metal contacts.[7] A strong electronic bond between metal and semiconductor materials is necessary for effective charge transfer doping and reduction of contact resistance; yet, at the same time, metal−semiconductor bonding results in Fermi level pinning. Many experimental and computational approaches to eliminate Fermi level pinning have been proposed including placing interlayers such as graphene and hexagonal boron nitride (h-BN) between the metal and TMDCs.[56−58] To investigate this depinning effect and corresponding influence on cross-plane carrier transport, we fabricated a MoS_2/h-BN/Au buried interface (case 3) by taking advantage of the Au-assisted dry-transfer technique (Figure 5a, fabrication details in Methods). Briefly, the presence of trilayer h-BN on MoS_2 prevents Fermi level pinning by avoiding direct contact with Au during evaporation (inset in Figure 5a and Figure S5a−d). The h-BN interlayer not only helps achieve a depinned contact interface but also helps in strain relaxation, as evident from the Raman spectrum of the monolayer MoS_2 case 3 interface (see Supplementary Figure S5e). This is expected since MoS_2 is not directly in contact with Au but rather with h-BN, which has a similar lattice constant and a weak van der Waals interaction.[59] In addition, there is no significant charge transfer between the metal and MoS_2 since they are physically separated by ∼1 nm of a wide-gap insulator. Figure 5b represents the surface potential map of this buried interface heterostructure, comprising regions of both monolayer (red) and bilayer (blue) MoS_2 spaced by ∼1 nm h-BN from the Au contact. Both regions showed obviously higher potential than the MoS_2 region without h-BN. The potential value of the monolayer (red dotted area) and bilayer (blue dotted area) MoS_2 with the case 3 interface recorded marginally different values compared to the case 1 (direct evaporation) interface (+50.6 mV for the monolayer MoS_2 case 3 and −5.57 mV for the bilayer MoS_2 case 3 interface). Corresponding work functions were 5.11 eV for monolayer MoS_2 case 3 and 5.16 eV for the bilayer case 3 interface. The values were between those measured for case 1 (direct evaporation) and case 2 (direct exfoliation) MoS_2 monolayers. This verifies that the depinned MoS_2 work function is very different from that of the case 1 (direct evaporation) interface. We want to note that there is an unexpected local strain during h-BN transfer, leading to a wrinkle (stripe in the potential map) across the h-BN and case 3 interface. Likewise, trapped air/hydrocarbon bubbles may also cause potential turbulence. TEPL further reveals that the monolayer MoS_2 case 3 interface is electronically isolated from the Au and emits high PL, while the PL from all other regions is quenched, including from bilayer MoS_2 (see Supplementary Figure S5f). Considering the above, it is clear that the electrical properties of the case 3 interface are fundamentally different because effects from neither Fermi level pinning nor strain are manifest throughout the MoS_2 flake. To understand better, we performed conductive AFM measurement by sweeping the applied voltage to the sample from −2.5 to 3 V (Figure 5c−f). Overall, the case 3 interface showed lower conductance than the directly contacted region (see Supplementary Figure S6b) as expected. Interestingly, however, the conductance was strongly dependent on MoS_2 layer number in the negative bias (Figure 5c top, d). Conduction through bilayer MoS_2 starts to increase at lower overpotential as compared to monolayer MoS_2. This is attributed to band alignments of these metal insulator semiconductor tunnel junctions where charge transport is over the barrier and, hence, band alignment of the semiconductor with the barrier insulator is critical. Compared to the monolayer MoS_2 band gap, the bilayer MoS_2 band gap is lowered by a conduction band decrease of ∼0.1 eV and valence band increase of ∼0.2 eV.[54] Moreover, it has been reported earlier that h-BN/MoS_2 alignment imparts a

https://dx.doi.org/10.1021/acsnano.1c00708
ACS Nano 2021, 15, 5618−5630

large barrier height for electrons but is negligible for hole transport.[60] Therefore, the current under negative bias results not from tunneling but rather from hole diffusion through the band inversion (Figure 5e). Note that after band inversion by sufficient voltage (−2.5 V), both regions reached similar conductance (Figure S6a). On the positive voltage side, similar conductance is observed throughout, regardless of MoS_2 thickness (Figure 5c bottom, d). Further, the current value was smaller compared to hole conduction. This can be attributed to the through-barrier (trilayer *h*-BN) tunneling mechanism for charge transport (Figure 5f) in a metal−insulator−semiconductor junction where the band gap of the semiconductor makes no significant difference. The tunneling behavior was further verified by introducing thicker *h*-BN barrier layers between MoS_2 and Au (see Supplementary Figure S7), which shows clear dependency on *h*-BN barrier thickness, independent of the number of MoS_2 layers, further verifying our claims.

To further enrich our understanding of the MoS_2−metal interface, we have generalized our scheme to other metal contacts aside from Au using the same transfer technique of template stripping. This technique is applicable to other metals such as In and Ag (Figures 6a and S8a), which have a reduced tendency to form oxides in contrast to other common contact metals. Further, both In and Ag have been evaluated in the past as contact metals for MoS_2. In particular, a recent demonstration of In/Au alloy or In contacts with monolayer MoS_2 revealing low contact resistance[11,61] motivates investigation of this contact type. As indicated in Figure 6a, the In/Au case 1 (direct evaporation) interface was also flipped over and shows a flat surface. Details of evaporation and stripping of the In/Au layer from the SiO_2/Si wafer are provided in the Methods and Supporting Information. A surface potential map of the In/Au alloy contact indicates that electronically uniform contact was formed throughout the monolayer region (Figure 6b). The high potential of +114 mV at the buried interface region was observed. It is attributed to the low work function of In (4.12 eV) immediately beneath the MoS_2 layer.[62] Interestingly, the potential of the In/Au substrate was lower than the In−monolayer MoS_2 case 1 (direct evaporation) interface and similar to that of the Au substrate (~0 V). Therefore, the potential map contrast (Figure 6b) is opposite the contrast of the pure Au contact buried interface (Figure 3a). This indicates that Au atoms are the dominant surface facing species at the In/Au substrate, while the buried interface with MoS_2 maintains In as the primary contact element facing MoS_2. We speculate that the diffusion rate of Au on MoS_2 during annealing is different from SiO_2 for such a condition to arise. Near-field and far-field Raman spectra were collected *via* TERS to investigate strain and charge transfer effects at this In−Au alloy interface with MoS_2 (Figure 6c). Similar to the buried interface with pure Au, the far-field signal was suppressed, while the near-field signal was enhanced by the Purcell effect of the In/Au plasmonic nanocavity with the Au scanning probe tip. Strain analysis of the Raman peaks suggests a ~5% (tensile) strain at the In/Au interface with MoS_2, comparable to the Au buried interface. Finally, local conductance measurements reveal a linear *I*−*V* relationship which shows ohmic contact (Figure 6d). Interestingly, the *z*-directional conductance was much higher than the Au−MoS_2 case 1 (direct evaporation) interface and almost identical to that of the In/Au substrate (inset of Figure 6d), in agreement with prior reports of low contact resistance in In/Au contacted MoS_2 FETs.[11] Accordingly, the extracted out-of-plane resistivity reached 63 kΩ μm for the monolayer MoS_2 sample. The contact resistance of MoS_2−In/Au is higher than the previously reported value of 1−3 kΩ μm using FET devices.[11,61] These differences in the resistance values result from the large differences in contact areas sampled in the two methods of measurement. In an FET device, an ensemble average conductance is measured across a metal−semiconductor contact area of ~10 μm^2. While for our C-AFM measurement this area is 400 nm^2. The nanoscale contact area results in limiting the conductance value that can be truly measured. Further, our measurement technique is more direct and does not include any effects from the channel or underlying substrate as in the case of the FET.

Likewise, the Ag buried interface was also investigated, and, unlike Au and In/Au, Ag contacts show much higher contact resistance (see Supplementary Figure S8) despite the lower work function as compared to Au. This suggests that contact resistance is largely influenced by Fermi level pinning rather than metal work function. Fermi level pinning can be addressed by careful control over the interface structure and evaporation conditions. The Ag contacts applied *via* thermal evaporation unlike the e-beam-evaporated Au contacts likely created additional damage to the MoS_2 layer during metal cooling. For comparison, thermally evaporated Au contacts were characterized and demonstrated similar *I*−*V* curves and resistivity (see Supplementary Figure S8e), suggesting the contact application method strongly dictates the performance of the contact. This is also evident in the surface potential maps of thermally evaporated Au and Ag, where huge work function variation was observed, which was noticeably absent in e-beam-evaporated Au and In/Au (Supplementary Figure S8b,d and Figures 3a and 6b).

CONCLUSIONS

We report a thorough and comprehensive study on the buried interface of a prototypical 2D semiconductor (MoS_2) with 3D metals (Au, In/Au, and Ag). In particular, we investigate comparative differences between Au/MoS_2 contact formation *via* two different means: (1) direct Au evaporation on the semiconductor and (2) direct exfoliation of the semiconductor on freshly stripped Au. Using a combination of scanning probe techniques and far-field as well as near-field optical techniques we have directly probed the optical and electrical properties of a 2D semiconductor−metal interface and inferred the conclusions to understand the nature of contact resistance at this buried interface. Based on our observations and interpretation, direct metal evaporation is undoubtedly better in terms of providing an electrically uniform, homogeneous contact as compared to a direct exfoliated semiconductor on a metal surface. Direct metal evaporation results in large strain in the buried monolayer and bilayer MoS_2, which results in changes to band gap and corresponding electrical contact properties. Fermi level pinning is the dominant effect in direct metal evaporation, which also affects the surface potential of the second layer bilayer MoS_2. In contrast, electrical contact in directly exfoliated samples is spatially inhomogeneous and electrically poor (low conductance) overall with the exception of a few "electrically active regions" of low surface potential/high conduction. The presence of an isolating interlayer such as *h*-BN between the MoS_2 and Au relieves strain and depins the Fermi level on MoS_2. Use of soft metal contacts such as In/Au reveals that conductance through the buried interface can

https://dx.doi.org/10.1021/acsnano.1c00708
ACS Nano 2021, 15, 5618−5630

be improved. Likewise, use of thermally evaporated Au and Ag contacts suggests that conductance through the contact increases, suggesting the cooling and growth of the metal after landing on a semiconductor has a defining role to play in determining the contact resistance. It is clear from our observations that while direct metal evaporation is the favored method for making contacts with low interface resistance, direct metal evaporation also results in Fermi level pinning at the 2D semiconductor/3D metal interface. To overcome this drawback, one needs either an intermediate depinning barrier layer such as *h*-BN or a soft, nonreactive low-melting-point metal such as In. In addition, the nature of metal evaporation and postcondensation cooling on the semiconductor also has an important role to play in determining contact resistance. Our results suggest that e-beam evaporation in combination with use of ultrathin barrier layers and low-melting-point metals holds the most desirable recipe toward forming depinned, low-resistance contacts of bulk metals to 2D semiconductors.

In conclusion, we have performed a detailed scanning probe-based study of the buried 2D semiconductor/3D metal interface and identified various attributes of the interface that contribute to the quality of electronic contact at the interface. We have also identified various criteria related to evaporation conditions and materials needed to form low-resistance metal contacts to 2D semiconductors.

METHODS

Fabrication of the MoS_2–Metal (Au and Ag) Case 1 (Direct Evaporation) Interface. The sample fabrications process (Supplementary Figure S9) is identical to the process described in a previous paper.[22] Briefly, mono- and bilayer MoS_2 were mechanically exfoliated on a Si/SiO_2 substrate. A Au layer of 100 nm was deposited on as-exfoliated MoS_2 by either e-beam evaporator (Kurt J. Lesker PVD 75 PRO-Line e-beam evaporator) or a thermal evaporator (Kurt J. Lesker Nano 36 thermal evaporator). For Ag, a thermal evaporator was used (Kurt J. Lesker PVD 75–e-beam/thermal evaporator). The deposition rate was set to 0.2 nm/s under low pressure (5×10^{-7} Torr). Epoxy was applied on the Au layer, and another Si substrate was placed as a transfer substrate. After heating to 100 °C for 2 h, the transfer substrate was gently peeled off, resulting in buried MoS_2 on Au or Ag.

Fabrication of the MoS_2–In/Au Case 1 (Direct Evaporation) Interface. A 6 nm In layer and an 80 nm Au layer were evaporated on the as-prepared MoS_2 on Si/SiO_2 substrate by e-beam evaporator (Denton Explorer 18). The deposition rate was set to 0.2 nm/s with the substrate holder water cooled at 15 °C. The sample was annealed at 300 °C, N_2 ambient condition, for 3 h. Right after that, it was immersed in acetone and sonicated for 5 s. Using a blade, the edge of the transfer wafer was scratched so that it was able to peel off.

Fabrication of the MoS_2/h-BN/Au Case 3 Interface. First, few-layered MoS_2 was mechanically exfoliated on a Si/SiO_2 substrate. Few-layered *h*-BN was transferred on top of the MoS_2. It is followed by Au evaporation. After that, an identical process to case 1 (direct evaporation) was conducted.

Far-Field Reflectance Measurement. Reflectance from the sample was measured by illuminating a white light source on the sample and passing the reflected light through a 600 grooves/mm grating before collecting them in a LabRam-EVO Raman spectrometer. Reflectance acquired from the polished silver mirror with the same acquisition setting was used to normalize the reflectance from the sample to avoid any absorption from the gold substrate.

Kelvin Probe Force Microscopy and Conductive-AFM Measurement. An OmegaScope-R (AIST-NT) setup was used for KPFM and C-AFM measurement. For KPFM measurement, a Au tip was biased by 3 V and connected to a lock-in amplifier while the sample was grounded. The tip was calibrated with freshly cleaved HOPG. The Au substrate displayed a work function of 5.16 eV in both samples, indicating the Au layer was textured mainly along the (100) direction.[53] For the C-AFM measurement, the tip was grounded while the sample was connected to 10 MΩ series resistance and biased. *I*–*V* curves were collected and averaged from 6 × 6 points.

Tip-Enhanced Raman/Photoluminescence Measurement. An identical AFM setup as described above was coupled to a LabRam-EVO Raman spectrometer (Horiba Scientific), with a laser excitation at 633 nm and with a power of ∼460 μW. Au-coated OMNI-TERS probes (APP Nano) were used for all measurements.

Resistivity Calculation. To obtain the contact area between the tip and sample, a Herztian contact model was used as described in the literature.[63]

$$d^{3/2} = \frac{3}{4} F \frac{1}{E^*} r^{-1/2}$$

(d is dented thickness by applied force, F is applied force, E^* is reduced Young's modulus, r is tip radius)

$$\frac{1}{E^*} = \frac{1 - \nu_1^2}{E_1} + \frac{1 - \nu_2^2}{E_2}$$

(E is Young's modulus and ν is Poisson ratio).

The Young's modulus (Poisson ratio) of monolayer MoS_2 and Au are 270 GPa (0.27) and 106 GPa (0.3), respectively.[64,65] Based on the values, reduced Young's moduli of MoS_2/metal samples were calculated. On plugging the applied force in the equation during contact mode, d is obtained as 5.41×10^{-11} m. The contact area (S) was calculated by $S = 2\pi rd$.

van der Waals Corrected Density Functional Theory Calculation. We have performed all of the van der Waals corrected DFT calculations using the Vienna *ab initio* Simulation Package (VASP)[66,67] with projector-augmented wave (PAW)[68] pseudopotentials and the Perdew–Burke–Ernzerhof (PBE) exchange–correlation functional.[69] We have used 5 × 5 × 1 *k*-points for the optimization processes and 9 × 9 × 1 *k*-points for n-SCF calculations for the MoS_2–Au(111) composite as well as parent systems. A 25 Å vacuum is employed in the *z*-direction to avoid all unwanted interactions between the layers. A plane-wave basis set energy cutoff of 400 eV was used for the calculations, and the systems were optimized until forces on each atom were converged to less than 0.01 eV $Å^{-1}$. We have used a Γ-centered *k*-point mesh to calculate static phonon modes and Raman intensity. The dielectric constant and the optical absorption coefficient values of the composites are also calculated using VASP. The calculations use the direct interband dipolar transitions.

ASSOCIATED CONTENT

Supporting Information

The Supporting Information is available free of charge at https://pubs.acs.org/doi/10.1021/acsnano.1c00708.

Actual value of reflectance, deconvolution of Raman spectrum and Raman mode table, schematic representation of KPFM *vs* band alignment, cross-section HAADF STEM and EDS images, characterization of MoS_2/*h*-BN/Au case 3 interface and conductance, potential map of Ag case 1 (direct evaporation) interface and Au case 1 (direct evaporation) interface made from thermal evaporator, and schematic figure of metal-assisted transfer process (PDF)

AUTHOR INFORMATION

Corresponding Author

Deep Jariwala – *Electrical and Systems Engineering, University of Pennsylvania, Philadelphia, Pennsylvania 19104, United*

https://dx.doi.org/10.1021/acsnano.1c00708
ACS Nano 2021, 15, 5618–5630

States; orcid.org/0000-0002-3570-8768; Email: dmj@seas.upenn.edu

Authors

Kiyoung Jo − *Electrical and Systems Engineering, University of Pennsylvania, Philadelphia, Pennsylvania 19104, United States;* orcid.org/0000-0003-4587-234X

Pawan Kumar − *Electrical and Systems Engineering and Materials Science and Engineering, University of Pennsylvania, Philadelphia, Pennsylvania 19104, United States;* orcid.org/0000-0002-5764-2915

Joseph Orr − *Electrical and Computer Engineering, Villanova University, Villanova, Pennsylvania 19085, United States*

Surendra B. Anantharaman − *Electrical and Systems Engineering, University of Pennsylvania, Philadelphia, Pennsylvania 19104, United States*

Jinshui Miao − *Electrical and Systems Engineering, University of Pennsylvania, Philadelphia, Pennsylvania 19104, United States*

Michael J. Motala − *Air Force Research Laboratory, Materials and Manufacturing Directorate, Wright-Patterson AFB, Ohio 45433, United States; UES Inc., Beavercreek, Ohio 45432, United States*

Arkamita Bandyopadhyay − *Materials Science and Engineering, University of Pennsylvania, Philadelphia, Pennsylvania 19104, United States;* orcid.org/0000-0002-8511-4925

Kim Kisslinger − *Brookhaven National Laboratory, Upton, New York 11973, United States*

Christopher Muratore − *University of Dayton, Dayton, Ohio 45469, United States;* orcid.org/0000-0002-5555-9261

Vivek B. Shenoy − *Materials Science and Engineering, University of Pennsylvania, Philadelphia, Pennsylvania 19104, United States*

Eric A. Stach − *Materials Science and Engineering, University of Pennsylvania, Philadelphia, Pennsylvania 19104, United States;* orcid.org/0000-0002-3366-2153

Nicholas R. Glavin − *Air Force Research Laboratory, Materials and Manufacturing Directorate, Wright-Patterson AFB, Ohio 45433, United States;* orcid.org/0000-0002-9447-7509

Complete contact information is available at: https://pubs.acs.org/10.1021/acsnano.1c00708

Author Contributions

All authors contributed to this study. K.J. conducted the scanning probe technique measurement and wrote the manuscript. K.J. and J.O. fabricated the samples. P.K. contributed to *h*-BN transfer on MoS_2 and electron microscopy. S.B.A. contributed to reflectance measurement, and K.K. contributed to TEM sample preparation. J.M., M.M., C.M., and N.G. assisted with sample preparation including In and Au evaporation. A.B. and V.S. contributed to DFT calculations. E.A.S. supervised the electron microscopy. D.J. supervised the entire research and was the thought leader on the study along with K.J. All authors contributed to revising the manuscript and interpretation of data/results.

Notes

The authors declare no competing financial interest.

ACKNOWLEDGMENTS

D.J. and K.J. acknowledge primary support for this work by the Air Force Office of Scientific Research (AFOSR) FA9550-21-1-0035 and U.S. Army Research Office under contract number W911NF-19-1-0109. D.J. and J.M. also acknowledge partial support from and FA2386-20-1-4074. D.J., E.A.S., and P.K. acknowledge support from National Science Foundation (DMR-1905853) and support from University of Pennsylvania Materials Research Science and Engineering Center (MRSEC) (DMR-1720530) in addition to usage of MRSEC-supported facilities. The near-field work and metal evaporation were carried out at the Singh Center for Nanotechnology at the University of Pennsylvania, which is supported by the National Science Foundation (NSF) National Nanotechnology Coordinated Infrastructure Program grant NNCI-1542153. J.O. was supported by the NSF-REU program hosted by the NNCI at Penn. K.K. acknowledges support for TEM sample preparation at the Center for Functional Nanomaterials, Brookhaven National Laboratory, which is a U.S. DOE Office of Science Facility, at Brookhaven National Laboratory, under Contract No. DE-SC0012704. S.B.A. acknowledges support from Swiss National Science Foundation Early Postdoc Mobility Program (187977). N.G. acknowledges support of Air Force Office of Scientific Research grant FA9550-19RYCOR050.

REFERENCES

(1) Dimoulas, A.; Tsipas, P.; Sotiropoulos, A.; Evangelou, E. K. Fermi-Level Pinning and Charge Neutrality Level in Germanium. *Appl. Phys. Lett.* **2006**, *89*, 252110.

(2) Yin, X.; Chen, H.; Pollak, F. H.; Chan, Y.; Montano, P. A.; Kirchner, P. D.; Pettit, G. D.; Woodall, J. M. Photoreflectance Study of the Surface Fermi Level at (001) *N*- and *P*-Type GaAs Surfaces. *J. Vac. Sci. Technol., A* **2002**, *10*, 131−136.

(3) Himpsel, F. J.; Hollinger, G.; Pollak, R. A. Determination of the Fermi-Level Pinning Position at Si(111) Surfaces. *Phys. Rev. B: Condens. Matter Mater. Phys.* **1983**, *28*, 7014−7018.

(4) Jariwala, D.; Davoyan, A. R.; Wong, J.; Atwater, H. A. Van Der Waals Materials for Atomically-Thin Photovoltaics: Promise and Outlook. *ACS Photonics* **2017**, *4*, 2962−2970.

(5) Brar, V. W.; Sherrott, M. C.; Jariwala, D. Emerging Photonic Architectures in Two-Dimensional Opto-Electronics. *Chem. Soc. Rev.* **2018**, *47*, 6824−6844.

(6) Allain, A.; Kang, J.; Banerjee, K.; Kis, A. Electrical Contacts to Two-Dimensional Semiconductors. *Nat. Mater.* **2015**, *14*, 1195−1205.

(7) Xu, Y.; Cheng, C.; Du, S.; Yang, J.; Yu, B.; Luo, J.; Yin, W.; Li, E.; Dong, S.; Ye, P.; Duan, X. Contacts between Two- and Three-Dimensional Materials: Ohmic, Schottky, and *P-N* Heterojunctions. *ACS Nano* **2016**, *10*, 4895−4919.

(8) Schulman, D. S.; Arnold, A. J.; Das, S. Contact Engineering for 2D Materials and Devices. *Chem. Soc. Rev.* **2018**, *47*, 3037−3058.

(9) English, C. D.; Shine, G.; Dorgan, V. E.; Saraswat, K. C.; Pop, E. Improved Contacts to MoS_2 Transistors by Ultra-High Vacuum Metal Deposition. *Nano Lett.* **2016**, *16*, 3824−3830.

(10) Liu, Y.; Guo, J.; Zhu, E.; Liao, L.; Lee, S.-J.; Ding, M.; Shakir, I.; Gambin, V.; Huang, Y.; Duan, X. Approaching the Schottky-Mott Limit in van Der Waals Metal-Semiconductor Junctions. *Nature* **2018**, *557*, 696−700.

(11) Wang, Y.; Kim, J. C.; Wu, R. J.; Martinez, J.; Song, X.; Yang, J.; Zhao, F.; Mkhoyan, A.; Jeong, H. Y.; Chhowalla, M. Van Der Waals Contacts between Three-Dimensional Metals and Two-Dimensional Semiconductors. *Nature* **2019**, *568*, 70−74.

(12) Chhowalla, M.; Shin, H. S.; Eda, G.; Li, L.-J.; Loh, K. P.; Zhang, H. The Chemistry of Two-Dimensional Layered Transition Metal Dichalcogenide Nanosheets. *Nat. Chem.* **2013**, *5*, 263−275.

(13) Kappera, R.; Voiry, D.; Yalcin, S. E.; Branch, B.; Gupta, G.; Mohite, A. D.; Chhowalla, M. Phase-Engineered Low-Resistance Contacts for Ultrathin MoS_2 Transistors. *Nat. Mater.* **2014**, *13*, 1128−1134.
(14) Voiry, D.; Goswami, A.; Kappera, R.; Silva, C. D. C. C. E.; Kaplan, D.; Fujita, T.; Chen, M.; Asefa, T.; Chhowalla, M. Covalent Functionalization of Monolayered Transition Metal Dichalcogenides by Phase Engineering. *Nat. Chem.* **2015**, *7*, 45−49.
(15) Cho, S.; Kim, S.; Kim, J. H.; Zhao, J.; Seok, J.; Keum, D. H.; Baik, J.; Choe, D.-H.; Chang, K. J.; Suenaga, K.; Kim, S. W.; Lee, Y. H.; Yang, H. Phase Patterning for Ohmic Homojunction Contact in $MoTe_2$. *Science* **2015**, *349*, 625−628.
(16) Lin, Y.-C.; Dumcenco, D. O.; Huang, Y.-S.; Suenaga, K. Atomic Mechanism of the Semiconducting-to-Metallic Phase Transition in Single-Layered MoS_2. *Nat. Nanotechnol.* **2014**, *9*, 391−396.
(17) Schauble, K.; Zakhidov, D.; Yalon, E.; Deshmukh, S.; Grady, R. W.; Cooley, K. A.; McClellan, C. J.; Vaziri, S.; Passarello, D.; Mohney, S. E.; Toney, M. F.; Sood, A. K.; Salleo, A.; Pop, E. Uncovering the Effects of Metal Contacts on Monolayer MoS_2. *ACS Nano* **2020**, *14*, 14798−14808.
(18) Moe, Y. A.; Sun, Y.; Ye, H.; Liu, K.; Wang, R. Probing Evolution of Local Strain at MoS_2-Metal Boundaries by Surface-Enhanced Raman Scattering. *ACS Appl. Mater. Interfaces* **2018**, *10*, 40246−40254.
(19) Atkin, J. M.; Berweger, S.; Jones, A. C.; Raschke, M. B. Nano-Optical Imaging and Spectroscopy of Order, Phases, and Domains in Complex Solids. *Adv. Phys.* **2012**, *61*, 745−842.
(20) Smithe, K. K. H.; Krayev, A. V.; Bailey, C. S.; Lee, H. R.; Yalon, E.; Aslan, Ö. B.; Muñoz Rojo, M.; Krylyuk, S.; Taheri, P.; Davydov, A. V.; Heinz, T. F.; Pop, E. Nanoscale Heterogeneities in Monolayer $MoSe_2$ Revealed by Correlated Scanning Probe Microscopy and Tip-Enhanced Raman Spectroscopy. *ACS Appl. Nano Mater.* **2018**, *1*, 572−579.
(21) Park, K.-D.; Khatib, O.; Kravtsov, V.; Clark, G.; Xu, X.; Raschke, M. B. Hybrid Tip-Enhanced Nanospectroscopy and Nanoimaging of Monolayer WSe_2 with Local Strain Control. *Nano Lett.* **2016**, *16*, 2621−2627.
(22) Krayev, A.; Bailey, C. S.; Jo, K.; Wang, S.; Singh, A.; Darlington, T.; Liu, G. Y.; Gradecak, S.; Schuck, P. J.; Pop, E.; Jariwala, D. Dry Transfer of van Der Waals Crystals to Noble Metal Surfaces to Enable Characterization of Buried Interfaces. *ACS Appl. Mater. Interfaces* **2019**, *11*, 38218−38225.
(23) Wang, Q.; Deng, B.; Shi, X. A New Insight for Ohmic Contacts to MoS_2: By Tuning MoS_2 Affinity Energies but Not Metal Work-Functions. *Phys. Chem. Chem. Phys.* **2017**, *19*, 26151−26157.
(24) Mak, K. F.; Lee, C.; Hone, J.; Shan, J.; Heinz, T. F. Atomically Thin MoS_2: A New Direct-Gap Semiconductor. *Phys. Rev. Lett.* **2010**, *105*, 136805.
(25) Splendiani, A.; Sun, L.; Zhang, Y.; Li, T.; Kim, J.; Chim, C.-Y.; Galli, G.; Wang, F. Emerging Photoluminescence in Monolayer MoS_2. *Nano Lett.* **2010**, *10*, 1271−1275.
(26) Kim, R. H.; Leem, J.; Muratore, C.; Nam, S. W.; Rao, R.; Jawaid, A.; Durstock, M.; McConney, M.; Drummy, L.; Rai, R.; Voevodin, A.; Glavin, N. Photonic Crystallization of Two-Dimensional MoS_2 for Stretchable Photodetectors. *Nanoscale* **2019**, *11*, 13260−13268.
(27) Rahaman, M.; Rodriguez, R. D.; Plechinger, G.; Moras, S.; Schüller, C.; Korn, T.; Zahn, D. R. T. Highly Localized Strain in a MoS_2/Au Heterostructure Revealed by Tip-Enhanced Raman Spectroscopy. *Nano Lett.* **2017**, *17*, 6027−6033.
(28) Milekhin, A. G.; Rahaman, M.; Rodyakina, E. E.; Latyshev, A. V.; Dzhagan, V. M.; Zahn, D. R. T. Giant Gap-Plasmon Tip-Enhanced Raman Scattering of MoS 2 Monolayers on Au Nanocluster Arrays. *Nanoscale* **2018**, *10*, 2755−2763.
(29) Zhang, X.; Nan, H.; Xiao, S.; Wan, X.; Ni, Z.; Gu, X.; Ostrikov, K. Shape-Uniform, High-Quality Monolayered MoS_2 Crystals for Gate-Tunable Photoluminescence. *ACS Appl. Mater. Interfaces* **2017**, *9*, 42121−42130.
(30) Kravtsov, V.; Berweger, S.; Atkin, J. M.; Raschke, M. B. Control of Plasmon Emission and Dynamics at the Transition from Classical to Quantum Coupling. *Nano Lett.* **2014**, *14*, 5270−5275.
(31) Zhang, Y.; Voronine, D. V.; Qiu, S.; Sinyukov, A. M.; Hamilton, M.; Liege, Z.; Sokolov, A. V.; Zhang, Z.; Scully, M. O. Improving Resolution in Quantum Subnanometre-Gap Tip-Enhanced Raman Nanoimaging. *Sci. Rep.* **2016**, *6*, 25788.
(32) Chakraborty, B.; Bera, A.; Muthu, D. V. S.; Bhowmick, S.; Waghmare, U. V.; Sood, A. K. Symmetry-Dependent Phonon Renormalization in Monolayer MoS_2 Transistor. *Phys. Rev. B: Condens. Matter Mater. Phys.* **2012**, *85*, 161403.
(33) Lu, X.; Utama, M. I. B.; Wang, X.; Xu, W.; Zhao, W.; Owen, M. H. S.; Xiong, Q. Gate-Tunable Resonant Raman Spectroscopy of Bilayer MoS_2. *Small* **2017**, *13*, 1701039.
(34) Sun, Y.; Liu, K.; Hong, X.; Chen, M.; Kim, J.; Shi, S.; Wu, J.; Zettl, A.; Wang, F. Probing Local Strain at MX_2-Metal Boundaries with Surface Plasmon-Enhanced Raman Scattering. *Nano Lett.* **2014**, *14*, 5329−5334.
(35) Richard-Lacroix, M.; Zhang, Y.; Dong, Z.; Deckert, V. Mastering High Resolution Tip-Enhanced Raman Spectroscopy: Towards a Shift of Perception. *Chem. Soc. Rev.* **2017**, *46*, 3922−3944.
(36) Zhu, W.; Esteban, R.; Borisov, A. G.; Baumberg, J. J.; Nordlander, P.; Lezec, H. J.; Aizpurua, J.; Crozier, K. B. Quantum Mechanical Effects in Plasmonic Structures with Subnanometre Gaps. *Nat. Commun.* **2016**, *7*, 11495.
(37) Sun, M.; Zhang, Z.; Chen, L.; Sheng, S.; Xu, H. Plasmonic Gradient Effects on High Vacuum Tip-Enhanced Raman Spectroscopy. *Adv. Opt. Mater.* **2014**, *2*, 74−80.
(38) Zhang, C.; Chen, B. Q.; Li, Z. Y. Optical Origin of Subnanometer Resolution in Tip-Enhanced Raman Mapping. *J. Phys. Chem. C* **2015**, *119*, 11858−11871.
(39) Roelli, P.; Galland, C.; Piro, N.; Kippenberg, T. J. Molecular Cavity Optomechanics as a Theory of Plasmon-Enhanced Raman Scattering. *Nat. Nanotechnol.* **2016**, *11*, 164−169.
(40) Schmidt, M. K.; Esteban, R.; González-Tudela, A.; Giedke, G.; Aizpurua, J. Quantum Mechanical Description of Raman Scattering from Molecules in Plasmonic Cavities. *ACS Nano* **2016**, *10*, 6291−6298.
(41) Wang, R.; Li, J.; Rigor, J.; Large, N.; El-Khoury, P. Z.; Rogachev, A. Y.; Kurouski, D. Direct Experimental Evidence of Hot Carrier-Driven Chemical Processes in Tip-Enhanced Raman Spectroscopy (TERS). *J. Phys. Chem. C* **2020**, *124*, 2238−2244.
(42) Bhattarai, A.; Crampton, K. T.; Joly, A. G.; Wang, C. F.; Schultz, Z. D.; El-Khoury, P. Z. A Closer Look at Corrugated Au Tips. *J. Phys. Chem. Lett.* **2020**, *11*, 1915−1920.
(43) Wang, C. F.; O'Callahan, B. T.; Kurouski, D.; Krayev, A.; Schultz, Z. D.; El-Khoury, P. Z. Suppressing Molecular Charging, Nanochemistry, and Optical Rectification in the Tip-Enhanced Raman Geometry. *J. Phys. Chem. Lett.* **2020**, *11*, 5890−5895.
(44) Zhao, W.; Wu, Q.; Hao, Q.; Wang, J.; Li, M.; Zhang, Y.; Bi, K.; Chen, Y.; Ni, Z. Plasmon-Phonon Coupling in Monolayer WS_2. *Appl. Phys. Lett.* **2016**, *108*, 131903.
(45) Conley, H. J.; Wang, B.; Ziegler, J. I.; Haglund, R. F.; Pantelides, S. T.; Bolotin, K. I. Bandgap Engineering of Strained Monolayer and Bilayer MoS_2. *Nano Lett.* **2013**, *13*, 3626−3630.
(46) Gołasa, K.; Grzeszczyk, M.; Binder, J.; Bożek, R.; Wysmołek, A.; Babiński, A. The Disorder-Induced Raman Scattering in Au/MoS_2 Heterostructures. *AIP Adv.* **2015**, *5*, 077120.
(47) Liu, Q.; Li, X.; He, Q.; Khalil, A.; Liu, D.; Xiang, T.; Wu, X.; Song, L. Gram-Scale Aqueous Synthesis of Stable Few-Layered 1T-MoS_2: Applications for Visible-Light-Driven Photocatalytic Hydrogen Evolution. *Small* **2015**, *11*, 5556−5564.
(48) Geng, X.; Sun, W.; Wu, W.; Chen, B.; Al-Hilo, A.; Benamara, M.; Zhu, H.; Watanabe, F.; Cui, J.; Chen, T. Pure and Stable Metallic Phase Molybdenum Disulfide Nanosheets for Hydrogen Evolution Reaction. *Nat. Commun.* **2016**, *7*, 10672.
(49) Kim, J. H.; Lee, J.; Kim, J. H.; Hwang, C. C.; Lee, C.; Park, J. Y. Work Function Variation of MoS_2 Atomic Layers Grown with Chemical Vapor Deposition: The Effects of Thickness and the

https://dx.doi.org/10.1021/acsnano.1c00708
ACS Nano 2021, 15, 5618−5630

Adsorption of Water/Oxygen Molecules. *Appl. Phys. Lett.* **2015**, *106*, 251606.
(50) Kang, J.; Liu, W.; Sarkar, D.; Jena, D.; Banerjee, K. Computational Study of Metal Contacts to Monolayer Transition-Metal Dichalcogenide Semiconductors. *Phys. Rev. X* **2014**, *4*, 031005.
(51) Popov, I.; Seifert, G.; Tománek, D. Designing Electrical Contacts to MoS_2 Monolayers: A Computational Study. *Phys. Rev. Lett.* **2012**, *108*, 156802.
(52) Jariwala, D.; Sangwan, V. K.; Late, D. J.; Johns, J. E.; Dravid, V. P.; Marks, T. J.; Lauhon, L. J.; Hersam, M. C. Band-like Transport in High Mobility Unencapsulated Single-Layer MoS_2 Transistors. *Appl. Phys. Lett.* **2013**, *102*, 173107.
(53) Derry, G. N.; Kern, M. E.; Worth, E. H. Recommended Values of Clean Metal Surface Work Functions. *J. Vac. Sci. Technol., A* **2015**, *33*, 060801.
(54) Berg, M.; Keyshar, K.; Bilgin, I.; Liu, F.; Yamaguchi, H.; Vajtai, R.; Chan, C.; Gupta, G.; Kar, S.; Ajayan, P.; Ohta, T.; Mohite, A. D. Layer Dependence of the Electronic Band Alignment of Few-Layer MoS_2 on SiO_2 Measured Using Photoemission Electron Microscopy. *Phys. Rev. B: Condens. Matter Mater. Phys.* **2017**, *95*, 235406.
(55) Ouyang, B.; Xiong, S.; Jing, Y. Tunable Phase Stability and Contact Resistance of Monolayer Transition Metal Dichalcogenides Contacts with Metal. *npj 2D Mater. Appl.* **2018**, *2*, 13.
(56) Farmanbar, M.; Brocks, G. Controlling the Schottky Barrier at MoS_2/Metal Contacts by Inserting a BN Monolayer. *Phys. Rev. B: Condens. Matter Mater. Phys.* **2015**, *91*, 161304.
(57) Cui, X.; Shih, E.-M.; Jauregui, L. A.; Chae, S. H.; Kim, Y. D.; Li, B.; Seo, D.; Pistunova, K.; Yin, J.; Park, J.-H.; Choi, H.-J.; Lee, Y. H.; Watanabe, K.; Taniguchi, T.; Kim, P.; Dean, C. R.; Hone, J. C. Low-Temperature Ohmic Contact to Monolayer MoS_2 by van Der Waals Bonded Co/*h*-BN Electrodes. *Nano Lett.* **2017**, *17*, 4781−4786.
(58) Farmanbar, M.; Brocks, G. Ohmic Contacts to 2D Semiconductors through van Der Waals Bonding. *Adv. Electron. Mater.* **2016**, *2*, 1500405.
(59) Lee, Y.; Kumar, A.; Forte, J. D. S.; Chaves, A.; Roy, S.; Taniguchi, T.; Watanabe, K.; Chernikov, A.; Jang, J. I.; Low, T.; Kim, J. Boosting Quantum Yields in 2D Semiconductors *via* Proximal Metal Plates. **2020**, *arXiv:2012.15114*. arXiv.org e-Print archive. http://arxiv.org/abs/2012.15114 (accessed Dec 30, 2020).
(60) Xing, S.; Zhao, G.; Wang, J.; Xu, Y.; Ma, Z.; Li, X.; Yang, W.; Liu, G.; Yang, J. Band Alignment of Two-Dimensional *h*-BN/MoS_2 van Der Waals Heterojunction Measured by X-Ray Photoelectron Spectroscopy. *J. Alloys Compd.* **2020**, *834*, 155108.
(61) Kim, B.-K.; Kim, T.-H.; Choi, D.; Kim, H.; Watanabe, K.; Taniguchi, T.; Rho, H.; Kim, J.-J.; Kim, Y.; Bae, M. Origins of Genuine Ohmic van Der Waals Contact between Indium and MoS_2. *npj 2D Mater. Appl.* **2021**, *5*, 9.
(62) Michaelson, H. B. The Work Function of the Elements and Its Periodicity. *J. Appl. Phys.* **1977**, *48*, 4729−4733.
(63) Fu, D.; Zhou, J.; Tongay, S.; Liu, K.; Fan, W.; King Liu, T.-J.; Wu, J. Mechanically Modulated Tunneling Resistance in Monolayer MoS_2. *Appl. Phys. Lett.* **2013**, *103*, 183105.
(64) Bertolazzi, S.; Brivio, J.; Kis, A. Stretching and Breaking of Ultrathin MoS_2. *ACS Nano* **2011**, *5*, 9703−9709.
(65) Cao, Y.; Allameh, S.; Nankivil, D.; Sethiaraj, S.; Otiti, T.; Soboyejo, W. Nanoindentation Measurements of the Mechanical Properties of Polycrystalline Au and Ag Thin Films on Silicon Substrates: Effects of Grain Size and Film Thickness. *Mater. Sci. Eng., A* **2006**, *427*, 232−240.
(66) Kresse, G.; Furthmüller, J. Efficient Iterative Schemes for *ab initio* Total-Energy Calculations Using a Plane-Wave Basis Set. *Phys. Rev. B: Condens. Matter Mater. Phys.* **1996**, *54*, 11169−11186.
(67) Hobbs, D.; Kresse, G.; Hafner, J. Fully Unconstrained Noncollinear Magnetism within the Projector Augmented-Wave Method. *Phys. Rev. B: Condens. Matter Mater. Phys.* **2000**, *62*, 11556−11570.
(68) Kresse, G.; Joubert, D. From Ultrasoft Pseudopotentials to the Projector Augmented-Wave Method. *Phys. Rev. B: Condens. Matter Mater. Phys.* **1999**, *59*, 1758−1775.
(69) Perdew, J.; Burke, K.; Ernzerhof, M. Generalized Gradient Approximation Made Simple. *Phys. Rev. Lett.* **1996**, *77*, 3865−3868.

https://dx.doi.org/10.1021/acsnano.1c00708
ACS Nano 2021, 15, 5618−5630